Characterization of Nanomaterials in Electrochemistry

22

Giorgia Greco

Contents

Abstract

Establishing new protocol for nanomaterial characterization of functional materials is an important step in our knowledge for understanding the correlation between atomic changes and electrochemical performances. We propose a combination of different state-of-the-art techniques as a robust approach for nanomaterial characterization, which is suitable in structural refinements of nanocrystalline active systems. This technique of studying microscopic properties of nanomaterials includes XAS (X-ray absorption spectroscopy) ex situ

G. Greco (✉)
Department of Science, Uiversity of Roma Tre, Rome, Italy
e-mail: giorgiagreco80@gmail.com

M. Aliofkhazraei, A.S.H. Makhlouf (eds.), *Handbook of Nanoelectrochemistry*,
DOI 10.1007/978-3-319-15266-0_30

and in situ, XRD (X-ray diffraction), high-resolution TEM (transmission electron microscopy), and XRF (X-ray fluorescence). In particular, we are using the site-selective XAS (performed at international synchrotron radiation facilities) that is sensible to the local structure (up to 5–10 Å around photoabsorbing sites) for characterization of the nanomaterials with singular accuracy. An investigation of the local structure and chemical disorder dynamics of a commercial Pt-Co alloy nanocatalyst, used as electrode material in proton exchange membrane fuel cells (PEMFC), will be presented and discussed.

Keywords

Absorption spectra, clusters • EXAFS in condensed matter • Nanocrystalline materials in electrochemistry • Structure of nanocrystalline materials

Introduction

The study of alternative energy sources is one of the main research subjects. In particular, the nanomaterials developing for applications of energy devices are of great interest today. This interest is driven by physical properties and environmental advantages offered by the nanomaterial technology. For example, nanoparticles of platinum (Pt) used as catalyst in the polymer electrolyte membrane (PEM) fuel cells (FCs) exhibit significantly higher oxygen reduction reaction (ORR) electrocatalytic activities than the same bulk material. In fact, the active catalytic sites are on the surface of the active material (Pt active sites); the nanoscale dimensions increase considerably the ratio of *surface atoms/bulk atoms* so that a high increase in active area and a strong reduction of Pt amount (very expensive material) are obtained. So nanosize can strongly influence the mechanical and electrochemical properties of an active material.

However, a deep structural characterization of nanomaterials is not simple because of the sample nanoscale size; in fact, the nanomaterials are made by only few atoms, and more common characterization techniques could be not achievable. So new protocols for nanomaterial characterization for understanding the correlation between changes in the atomic ordering, changes, and (degradation of) performances are important to be established. This chapter is organized as:

- Section "Experimental Techniques: Theory" presents the main theoretical aspects of the experimental techniques used in the characterization protocol, namely, X-ray absorption spectroscopy (XAS), X-ray diffraction (XRD), X-ray fluorescence (XRF), and transmission electrons microscopy (TEM).
- Section "Experimental Techniques: Setups and Analysis Results" presents the details of the experimental setups allowing characterization of the nanomaterials.
- Section "EXAFS Analysis and Effect of Chemical Disorder" reports about the methodology used to perform Co-Pt nanomaterial atomic structure characterization.

Full characterization of the pristine material Pt-Co sample is discussed in light of results obtained combining experimental data with theoretical calculations.

- Appendix shows experimental setup allowing characterization of the samples and performance of experiments under in situ conditions. Experiments were performed at synchrotron ESRF (Grenoble).

Experimental Techniques: Theory

In this section, the main characteristics of those techniques, such as XAS, XRD, XRF and TEM will presented. The combination of all of these techniques represents a powerful atomic structure characterization methodology of active nanomaterials. In Table 1, the main informations obtained by the characterization techniques presented are shown.

X-ray Absorption Spectroscopy

One of the most powerful structural techniques that allows to investigate the neighborhood of a photo-absorber atom in a condensed medium is X-ray absorption spectroscopy (XAS) [1–4]. The absorption cross section above a deep core level excitation threshold presents oscillation characteristic of the compound being examined, due to interference effects in the transition matrix element, which in turn are related to a suitably projected density of the unoccupied electronic states. The development for XAS theory has been since the early 1970s, because of the rapid experimental advances obtained by the advent of synchrotron radiation, in particular for the extended X-ray absorption fine structure (EXAFS) [44–46]. The structural signal of EXAFS is defined as the relative oscillation with respect to a smooth total atomic cross section σ_0^t normalized to the atomic cross section of

Table 1 Summary of the main results that can be obtained with the characterization techniques presented in this chapter

Technique	Probe	Information about atomic structure	Results
XRD	X-rays	Long range order	Crystalline structure, primitive cell parameter, phase homogeneity, particle dimension
XAS	X-rays	Local structure	R = distances N = coordination number, σ^2 = Debye-Waller parameter
XRF	X-rays	Chemical components	Presence of impurities not detectable with other techniques
TEM	Electrons	Morphology and long range order	Crystalline structure, morphology of a particle, particle distribution, particle dimension

the edge under consideration σ_0, i.e., $\chi(k)=\left[\sigma(E)-\sigma_0^t(E)\right]/\sigma_0(E)$ where $k=\sqrt{2m(E-E_e)}$ is the modulus of the wave vector of photoelectron (E_e being the threshold energy). The contribution to $\chi(k)$ of each atom at a given distance R with is represented by an oscillating signal $A(k)\sin\left[2kR+\phi(k)\right]$.

This signal suggested the use of a Fourier transform technique [5–7]; in this way, the contributions from the coordination shells can be isolated. $A(k)$ is the amplitude and is characteristic of the backscattering atom. The dephasing term $\phi(k)$, which can be approximated with a linear function of k, is the sum of two independent functions associated with photo-absorber and backscatterer atoms, respectively, called "amplitude and phase transferability" [8]; this is at the basis of the standard method of EXAFS data analysis [1–4].

The photo-absorption process can be summarized as follows: a primary probe (a high-energy X-ray photon) interacts with a selected atom built in a certain structure. The photon excites a deep core electron that generates a free photoelectron that acts as a secondary probe. The photoelectron is in the continuum state with a defined energy; its wave function diffuses from the excited atom that strongly interacts (Coulomb interaction) with the surrounding atoms. The presence of neighboring atoms causes an effect in the absorption cross section. This can be calculated starting from the isolated atom in a perturbative scattering scheme. It is not possible to limit the expansion to single-scattering terms due to the strong electron-atom coupling, but multiple-scattering (MS) terms of the higher order should be included.

The presence of several atoms around the photo absorber can be probed by MS terms, so they probe the distribution functions of n particle. MS dominant effects are in the low kinetic energy region that corresponds to the X-ray absorption near edge structure (XANES). The MS contributions allow us to perform EXAFS data analysis based on theoretical calculations, GNXAS package [9].

Multiple-Scattering Expansion

For a model cluster, we can consider the problem of calculating the $\chi(k)$ which is relevant to the structure under investigation. The total many-body absorption cross section $\sigma_{tot}(\omega)$ under general conditions can be written in the following way:

$$\sigma_{tot}(\omega)=\int_0^\infty \sigma(\omega-\omega')A_c(\omega')d\omega'=\sigma(\omega)|S(\omega)|^2 \tag{1}$$

For transitions to a dipole sorted final state of angular momentum l_0 polarization averaged [10, 11], the XAS cross section is

$$\sigma(\omega)=\sigma_0\left[\mathcal{J}\frac{1}{\mathcal{J}(t_0^{l_0})}\frac{1}{2l_0+1}\sum_{m_0}\left[T(I-GT)^{-1}\right]_{0,0}^{L_0,L_0}\right] \tag{2}$$

With good approximation, this equation is valid for complex potentials, while for real potentials, it is exact. A complete discussion is referred to Ref. [12].

T and G are the atomic scattering and propagator matrices in a local basis and σ_0 is the atomic cross section. One element of these matrices is identified by the indices

i and j overrunning the several atomic centers in the matter and by angular momenta set L, L' (where $L=l, m$). Every atomic index couple locates an "atomic" block of the matrices. So the T matrix is diagonal block ($T_{i,j}=t_i\delta_{i,j}$), and for the atom at center i, the scattering matrix is diagonal in the L indices $\left(t_i^{L,L'}=t_i^l\delta_{L,L'}\right)$ in the MT approximation, since in the scattering from a single site, the angular momentum is conserved. In terms of the lth potential phase shift δ_i^l at site i, one has $t_i^l=\exp\left(i\delta_i^l\right)\sin\left(\delta_i^l\right)$. By solving the Schrödinger equation, these quantities can be calculated.

The matrices G_{ij} contain geometrical information on the atoms i and j dispositions regardless of their scattering power. In fact, looking at Eq. 1, the G matrix appears in an inverse expression $(I-GT)^{-1}$; for this reason, the effects of different structural dispositions on the cross section can be decoupled.

Assumed that the norm of the GT matrix (maximum modulus of its eigenvalues) is less than one, $\|GT\|<1$; in this case, the formal matrix expansion $T(I-GT)^{-1}=T(I+GT+GTGT+GTGTGT+\ldots.)$ is convergent and gives rise to the familiar MS series [11]. The series include χ_n terms defined for each order of scattering n according to the number of propagators G contained in each term of the series.

The χ_n represents the oscillating signals related to the scattering path that starts and ends at the origin with the constraint that successive sites must be distinct:

$$\chi_n\left(k\right)=A\left(k,R\right)\sin\left[kR_p+\phi\left(k,R\right)\right] \tag{3}$$

where A and ϕ are smooth functions of k and of the geometrical parameters R. The pertinent signal frequency is determined by the path length R_p.

So XAS cross sections of cluster of N atoms are possible to be calculated. Given the photo absorber "0" and the surrounding atoms i, j, k, …., let us skip some steps (details in Ref. [13]); total cross section expansion in the n-body cross sections is useful as

$$\begin{aligned}\sigma\left(0,i,j,\ldots.,n\right)=\sigma_0+\sum_i\sigma^{(2)}\left(0,i\right)+\\+\sum_{(i,j)}\sigma^{(3)}\left(0,i,j\right)+\sum_{(i,j)}\sigma^{(4)}\left(0,i,j,k\right)+\ldots\\+\sigma^{(n)}\left(0,i,j,\ldots.,n\right)\end{aligned} \tag{4}$$

Let us introduce the dimensionless quantities $\gamma^{(n)}=\sigma^{(n)}/\sigma_0$, which represent the irreducible n-body contributions to the EXAFS, Eq. 5 reduces for the dimensionless experimental structural signal to an equivalent expansion χ:

$$\begin{aligned}\chi\left(0,i,j\ldots.n\right)=\gamma_0+\sum_i\gamma^{(2)}\left(0,i\right)+\\+\sum_{(i,j)}\gamma^{(3)}\left(0,i,j\right)+\sum_{i,j,k}\gamma^{(4)}\left(0,i,j,k\right)+\ldots\\+\gamma^{(n)}\left(0,i,j\ldots.,n\right)\end{aligned} \tag{5}$$

So we obtain a linear relationship between structure (in terms of 2, 3, 4, … n-body distributions) and signal.

If the system is a cluster (finite), Eq. 6 contains a finite number of terms becoming a series only in the case of a system with an infinite number of atoms.

In this case, it is expected anyway, due to mean-free-path effects, that the higher-order n-body terms are smaller than the lower-order ones and that the series has very good convergence properties.

In GNXAS package, the equation solution of structural problem 1 used is based on the MS calculations for the $\gamma(n)$, substituting in equations

$$\gamma^{(2)}(0,i) = \sigma(0,i)/\sigma_0 - 1 \tag{6}$$

and

$$\gamma^{(3)}(0,i,j) = \sigma(0,i,j)/\sigma_0 - \sigma(0,j)/\sigma_0 - \sigma(0,i)/\sigma_0 - 1 \tag{7}$$

the respective series of MS. Because of the matrices structure in two blocks, for the two-body term 6, solely *TG* even powers give a contribution, and the matrix expression is

$$\left(\begin{Bmatrix} t_0 & 0 \\ 0 & t_i \end{Bmatrix} \sum_{n=1}^{\infty} \left[\begin{Bmatrix} 0 & G_{0,i} \\ G_{i,0} & 0 \end{Bmatrix} \begin{Bmatrix} 0 & G_{0,i} \\ G_{i,0} & 0 \end{Bmatrix} \right]^n \right)^{0,0} \tag{8}$$
$$= t_0 G_{0i} t_i G_{i,0} t_0 + t_0 G_{0i} t_i G_{i,0} t_0 G_{0i} t_i G_{i,0} t_0 + \ldots.$$

The MS expansion, pictorially represented in Fig. 1a, results

$$\gamma^{(2)}(0,i) = \chi_2^{(0i0)} + \chi_4^{(0i0i0)} + \chi_6^{(0i0i0i0)} + \ldots \tag{9}$$

The necessary number of MS terms depends on bond distance, atomic numbers, and *k* range involved.

In the region of EXAFS signal, terms up to χ_6 for short bonds are found important while χ_4 is usually sufficient for longer bonds. The configurational average is even efficacious in the damping of MS higher-order signals. Moreover, the MS

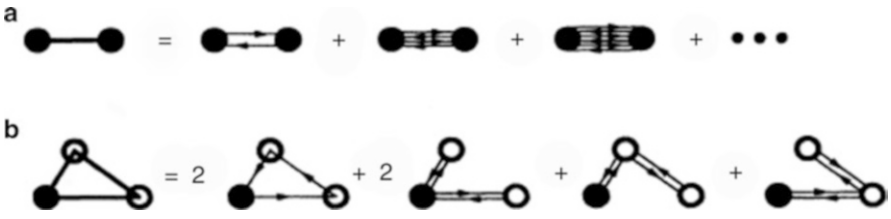

Fig. 1 (**a**) Schematic view of the expansion MS for $\gamma^{(2)}$ signals that include terms up to χ_6. The $\gamma^{(2)}$ signals regard for an infinite number of MS paths. (**b**) Schematic view of the MS expansion for $\gamma^{(3)}$ signals that include terms up to χ_4. The $\gamma^{(3)}$ signals regard for an infinite number of MS paths (From reference [13])

expansion is peculiar for $\gamma^{(2)}$, the following terms have main frequencies multiple of $2R$, R that is the distance between atoms 0 and i. As a result, there is a big difference of frequency between the main term χ_2 and the next order correction χ_4.

Starting from Eq. 7, the MS succession for $\gamma^{(3)}(0, i, j)$ can be derived but is more complex (see Ref. [13]). By carrying out the products of matrix, for three-body part, we can obtain terms of any order in the scattering that contain all three atoms 0, i, and j or simply 0 and i or 0 and j.

These two contributions are exactly compensated by the terms resulting from the $\gamma^{(2)}$ signals that appear with negative sign. So in this way, $\gamma^{(3)}_{0,i,j}$ is equal to the sum of all possible MS signals that involve "all and only" 0, i, and j in any possible sequence. The terms with lowest order are the χ_3 signals that correspond to the sequences O–i–j–O and O–j–i–O. Due to symmetry of time reversal, the two signals coincide and only one of them can be considered with double degeneracy. This happens for all the paths. When the paths are reversed, they generate a different sequence. These symmetric sequences under inversion happen conversely only once (single degeneracy). In Fig. 1b, $\gamma^{(3)}$ signal is depicted. So not taking into account the triangle geometry, for the χ_n terms successive starting from $R_{Oi}+R_{ij}+R_{j0}$, the possible paths are multiple and bring a continuous distribution of dominant frequencies. As results, $\gamma^{(3)}$ presents a regular oscillation in k space. Examples of the importance of χ_5 and χ_6 terms have been reported [14]. In general in the low-k range, these higher-order terms contribute producing a total signal modification.

Configurational Average of the Signal

Now, there are different approaches for calculating the MS contribution configurational damping. Reproduce the signal intensity correctly is not simple and is crucial. In particular, GNXAS package uses the algorithm based on an advanced theory, which takes into account the related configurations of vibration of N atom [11] and spherical wave effects. In the small disorder case, the effect of configurational disorder and/or thermal vibrations can be calculated easily. In fact it has represented by an isolated and well-defined peak and the distribution function does not need Gaussian. Also the thermal broadening of crystalline and molecular peaks are included such as the case of low structural disorder. In case of a larger disorder the peaks are not well defined, but are broaden and overlapped. For both of these cases the signal can be reproduced and written in terms of an amplitude and a phase. Synthesists and skipping some steps the theoretical signal can be written in a more general case as a combination of terms for N neighboring atoms, and with thermal and static disorder of σ^2 (mean-square disorder in R). Then, considering a real system, we will have the different types of neighboring atoms at different distances:

$$\chi(k) = \sum_i \frac{N_i A_i(k) e^{-2k^2\sigma_i^2}}{kR_i^2} \sin\left[2kR_i + \delta_i(k)\right] \tag{10}$$

Considering a damped wave function (photoelectron mean free path that includes core-hole lifetime) and amplitude reduction term S_0^2 which takes into

account the relaxation of all the other electrons, we obtain an equation modeling and interpreting EXAFS:

$$\chi(k) = \sum_i \frac{N_i S_0^2 A_i(k) e^{-2R_j/\lambda(k)} e^{-2k^2\sigma_i^2}}{kR_i^2} \sin\left[2kR_i + \delta_i(k)\right] \tag{11}$$

If we know $A(k)$, $\delta(k)$, and the mean free path $\lambda(k)$ by EXAFS analysis, we can determine:

1. R distance to neighboring atom
2. N coordination number of neighboring atom
3. σ^2 mean-square disorder of neighbor distance

X-ray Diffraction Techniques

The elastic scattering of X-rays from structures that have long range order is the base on X-ray diffraction (XRD) techniques. The most comprehensive description of scattering from crystals is given by the dynamical theory of diffraction [15].

- XRD of a single crystal is a technique used to determine the complete structure of crystalline materials, such as simple inorganic solids and complex macromolecules (proteins).
- Powder diffraction is a characterization technique used for establishing the crystal structure, crystallite size (grain size), and preferred orientation in polycrystalline or powdered solid samples. Powder diffraction is frequently used to identify substances, by comparing diffraction data against a database maintained by the International Center for Diffraction Data. P

Scherrer Equation

The effects of size and strain can be often separated in the powder diffraction technique, in particular when the size broadening is independent of q (K = 1/d), strain broadening increases with increasing q-values. But frequently, there will be both size and strain broadening. By combining the two equations, it is possible to separate these with the Hall-Williamson method:

$$B \cdot \cos(\theta) = \frac{K\lambda}{D} + \eta \cdot \sin(\theta) \tag{12}$$

Therefore, when we plot $B{\cdot}\cos(\theta)$ vs. $\sin(\theta)$, we obtain a straight line with slope η and intercept $\frac{k\lambda}{D}$. This expression is the combination of the Scherrer equation [16] for size broadening and the Stokes and Wilson expression for strain broadening. The η value is the strain in the crystal structure and the D value features the size of the crystallites. K is constant typically ranges from 0.8 to 1.39.

X-ray diffraction and crystallography use a shape factor to correlate in a solid the size of sub-micrometer particles or crystallites to the peak broadening in a diffraction pattern: the Scherrer equation,

$$D = \frac{K\lambda}{\beta \cos\theta} \tag{13}$$

where K is the shape factor, λ is the X-ray wavelength (typically ~ 1 Å), β is the line broadening at half the maximum intensity (FWHM) in radians, and θ is the Bragg angle; D is the crystalline mean size (ordered) domains that may be equal to or smaller than the grain size. The shape factor is dimensionless and has a typical value of ~0.9, but it can vary with the real crystallite shape. It is important to know that the Scherrer equation is limited to the particles in nanoscale. It cannot be applicable to particles larger than about 0.1 μm (the Scherrer formula can calculate only a lower bound on the particle size; in fact, the broadening of the diffraction peak can include a variety of factors; one most important of these is inhomogeneous strain and instrumental effects).

X-ray Fluorescence

Bombarding a material with high-energy X-rays, it will emit a characteristic "secondary" X-ray, which is called X-ray fluorescence (XRF) (or fluorescent). This phenomenon is largely used for elemental and chemical analysis, particularly in the investigation of solid materials like glass, metals, building materials, and ceramics.

X-ray fluorescence spectroscopy is useful for knowing what chemical components are present in a sample, even if those components are in small quantities and in amorphous phase.

The electronic orbital has a characteristic energy for each element. After inner electron excitation in the continuum by an energetic photon given by a primary radiation source, an electron from an outer shell drops into its place. The ways in which this can happen are limited. The main transitions are the following: an $L \rightarrow K$ transition is traditionally called K_α, an $M \rightarrow K$ transition is called K_β, an $M \rightarrow L$ transition is called L_α, and so on. Any transition produces a fluorescent photon with a characteristic energy equal to the difference in energy of the initial and final orbital. The wavelength of this fluorescent radiation can be calculated from Planck's Law:

$$\lambda = h \cdot c / E \tag{14}$$

This radiation can be analyzed in two ways: first by sorting the energies of the photons (energy-dispersive analysis) and second by separating the wavelengths of the radiation (wavelength-dispersive analysis). Once classified, the intensity of each radiation is related to the amount of each element in the material. This is a powerful technique widely used in analytical chemistry.

Imaging Methods

Transmission electron microscopy (TEM) utilizes imaging methods based on information that are contained in the electron waves exiting from the sample forming an image. The used lenses permit the correct electron wave distribution onto the viewing system. The image intensity, I, can be considered proportional to the time-averaged amplitude of the electron wave function, where the exiting wave forming the exit beam is called Ψ [17]:

$$I(x) = \frac{k}{t_1 - t_0} \int_{t_0}^{t_1} \Psi \Psi^* dt \tag{15}$$

Thus, there are different imaging methods trying to simplify the exiting electron waves in a useful form to obtain information regarding the sample or beam itself. The previous equation evidences that the observed image depends not only on the amplitude of beam but also on the electron phase, while at lower magnifications, phase effects can be ignored. But imaging at higher resolution requires higher energies of incident electrons and thinner samples. Hence, Beer's law effect [18] cannot be applicable at the sample longer, rather it is possible to model the sample as an object which does not change the incoming electron wave function amplitude but the phase of the incoming wave; for sufficiently thin samples, the phase effects dominate and this model is known as a pure phase object [17, 19].

High-Resolution Imaging

When an imaging formation process occurs [20], running the electron beam run through the microscope and different phenomena can be resulting, they can be distinguished (see Fig. 2a):

- In the plane of object, diffraction phenomena
- The image formation in the objective lens back focal plane
- The interference of diffracted beam in the image plane of the objective lens

Due to the Huygens' principle, the electron wave function $\phi_{ex}(r)$ at the exit face of the object can be considered a planar source of spherical waves. In the reciprocal vector **g** direction, the amplitude of diffracted wave is given by objected function Fourier transformation:

$$\psi(g) = J_g \psi(r) \tag{16}$$

In the diffraction pattern, the intensity of the distribution is given by $|\psi(g)|^2$ in the objective lens back focal plane.

$$\left|\psi(g)\right|^2 = \left|J_g \psi(r)\right|^2 \tag{17}$$

If the objective is periodic, the diffraction pattern, the square of the FT of object function, will consist of sharp spots. In the second stage of the imaging process,

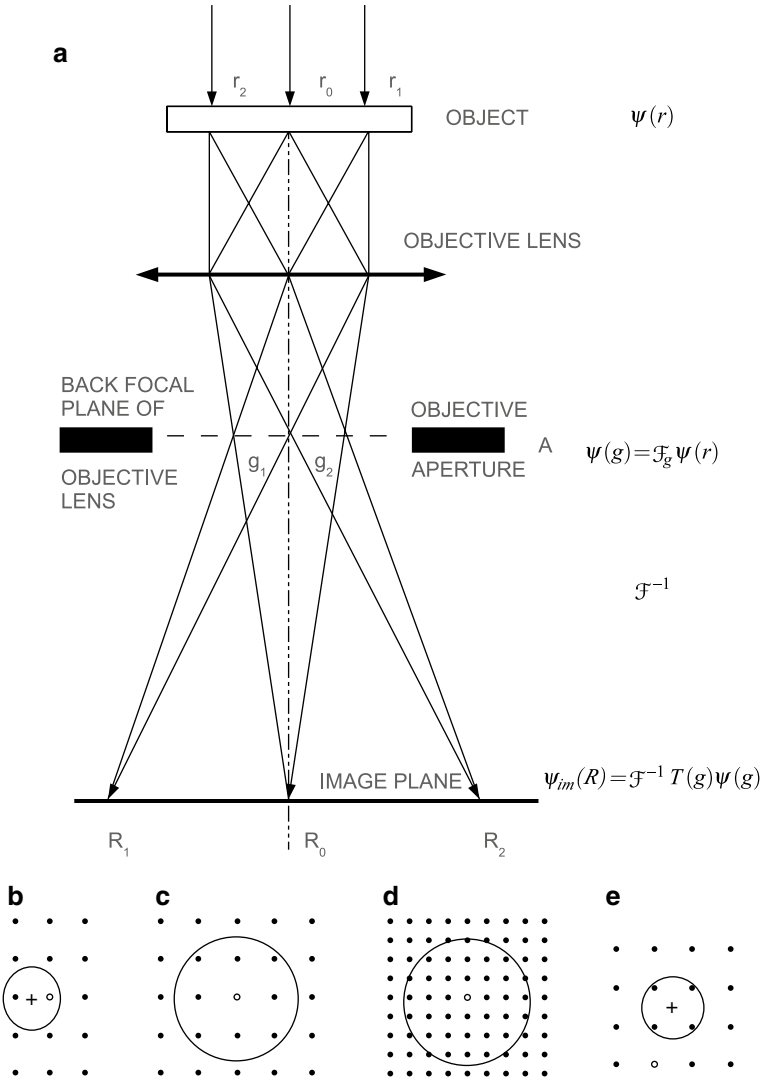

Fig. 2 (**a**) Image formation in a electron microscope; (**b**–**e**) scheme of diffraction patterns and aperture configurations; +, optical axis; o, undiffracted beam; O, objective aperture A as placed in (**a**) (Adapted from reference [21])

considered a system of lenses the back focal plane acts as a sequence of Huygens' spherical wave sources which interfere in the image plane. Inverse Fourier transform describes this stage in the imaging process that makes an enlarged object function $\psi(R)$. Finally, in the image plane, the intensity is given by $|\psi(R)|^2$. In the second step during the image formation, described by the inverse Fourier transform, the electron beam suffers phase shift $\chi(g)$ with respect to the central beam. This phase shift is

due to spherical aberration and defocus and damped by incoherent damping function $D(\alpha, \Delta, g)$, so at the image plane, the wave function $\psi_{im}(R)$ is obtained as

$$\psi_{im}(R) = J^{-1}T(g)\psi(g) \tag{18}$$

where $T(g)$ is the contrast transfer function (CTF) of thin phase object. $T(g)$ includes damping envelop $D(\alpha, \Delta, g)$ and phase shift $\chi(g)$:

$$\chi(g) = \pi\varepsilon\lambda g^2 + \pi C_s\lambda^3 g^4 / 2 \quad T(g) = D(\alpha,\Delta,g)\exp\left[i\chi(g)\right]$$

where α is the convergent angle of the incident electron beam and Δ is the half width of the defocus spread ε due to chromatic aberration. For the details, consult references [21–23].

The main experimental techniques in common use at present in the field of conventional high-resolution electron microscopy, in phase contrast, are given in Fig. 2b–e [20]. The different imaging modes are determined by the size and geometrical position of the objective aperture in the focal plane back of the objective lens. An image of a lattice fringe is obtained, if only one (or a few) diffracted beams interfere with the unscattered beam (aperture like type b). The period of the fringes corresponds to the interplanar spacing of exited beam. Using aperture type c, many beam images will be observed. For thin crystal having large unit cell parameters under experimental conditions, obtained using type d, the "structure image" could be obtained if the micrograph is directly interpreted in terms of projected atomic arrangement of the crystal structure. If particular diffracted beam of interest interferes and all other beams are excluded, a dark-field lattice image is formed, aperture type e (see Fig. 2).

Experimental Techniques: Setups and Analysis Results

In this section, some important technical and scientific details about the experimental devices used for microstructure characterization of the nano-nanomaterial under various conditions will be discussed.

Some experiments performed on a nanocatalyst sample in different laboratories such as at synchrotron radiation (SR) facilities will be shown as examples.

The order in which the experimental techniques are presented reflects the ideal sequence of material science characterization technique used for nanoparticle analysis.

TEM Imaging

The first important characterization regards the knowledge of mean nanoparticle size, their distribution, if they are well dispersed and have a homogeneous crystalline structure. This information can be obtained from HRTEM images (transmission high-resolution electron microscopy), looking at the individual particle shape and structure. Here, we would like to show an example: the nanocatalyst under

consideration is composed of Pt-Co alloy metal nanoparticles dispersed on a matrix of Vulcan. HRTEM images have been collected using a JOEL JEM-2100F at the Institute of Mineralogy and Physics of Condensed Matter (IMPMC) of UPMC University, Paris.

Given the size of nanoparticles, we have chosen to perform TEM measurements by JOEL JEM-2100F. In particular by the obtained images, we are able not only to calculate the average particle diameter but also to observe the crystal structure and calculate the distance between crystalline planes, information which allows us to observe possible phase separations. The JEM-2100F is equipped also with other techniques such as scanning transmission electron microscopy (STEM) and energy-dispersive X-ray spectroscopy (EXD) from which we did the elemental analysis and chemical characterization of the samples.

For TEM experiments, sample preparation is a complex procedure. In fact, TEM specimens have to be at most hundreds of nanometers thick, because of the electron beam that interacts quickly with the sample, and this effect increases in first approximation with atomic number squared (z^2) [18].

Quickly preparation by the deposition of a dilute sample containing the specimen onto support grids can be used for such nanomaterials, such as powders like Pt-Co/C nanocatalysts or nanotubes, that have dimensions small enough to be electron transparent.

An example of particle size distribution, on the basis of TEM image analysis, using the ImageJ program, (ImageJ, Version 1.38x, Wayne Rasband, National Institutes of Health, USA) has been obtained and presented. The profiles of 500 randomly selected quasi-spherical particles have been taken under a consideration. A typical TEM image of Pt-Co nanoparticles with almost a spherical shape is shown in Fig. 3a–c presenting their size distribution, which is asymmetric and shows a tail extended to large-sized nanoparticles. A log-normal model can be reproduced quite accurately in this size distribution.

The fast Fourier transforms (FFTs) of high-resolution TEM (HRTEM) images [25, 26] calculated by ImageJ program were compared with simulated electron diffraction patterns of ordered Pt_3Co (space group $Pm\bar{3}m$) and ordered Pt-Co (space group $P4/mmm$) [27]. In the FFT images, each spot of diffraction pattern represents a set of equal spacing planes whose direction is normal and corresponds to the straight line connecting this diffraction spot with the transmitted one. This straight length line is proportional to the reciprocal of the interplanar distance. ImageJ program allows the calculation from FFT images of the interplanar distance and the angle between atomic planes that permits in the HRTEM images indexing of lattice fringes (see Fig. 3 in the inset).

X-ray Diffraction and X-ray Fluorescence

From X-ray diffraction technique, information on mean crystalline structure, multiple phases, mean nanocrystals size, and alloy stoichiometry can be obtained. Unlike the TEM results, the obtained informations from XRD are averaged all

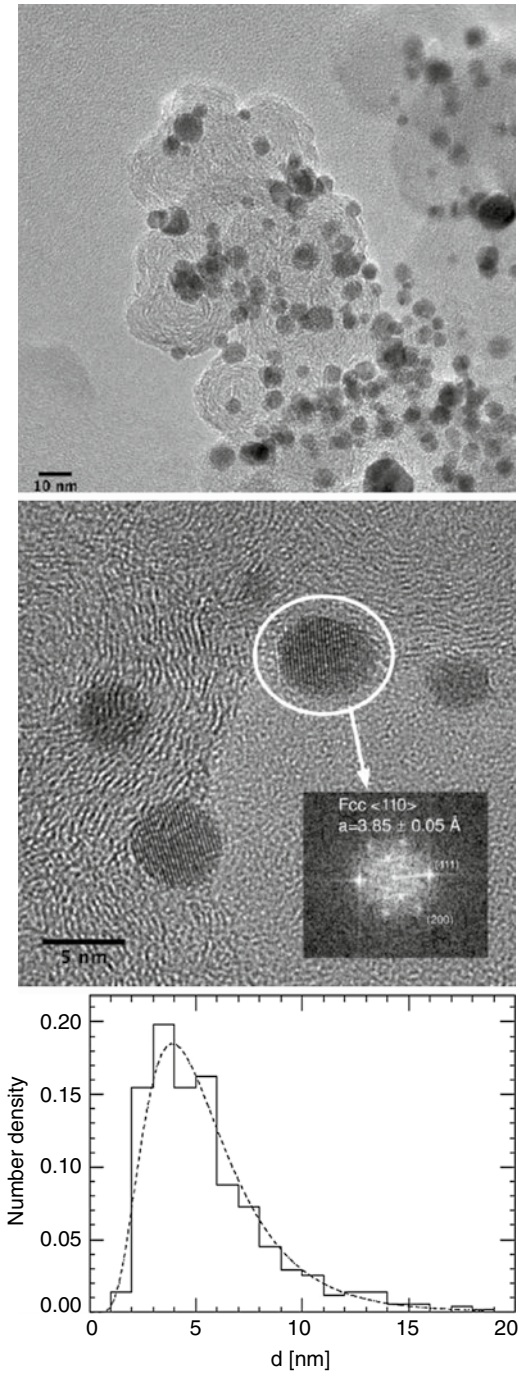

Fig. 3 (*Top*) TEM and (*middle*) HRTEM images of platinum cobalt nanoparticles supported on Vulcan (E-TEK™). In the *inset*, lattice reflections are shown at fast Fourier transform (FFT) of the HRTEM image of nanoparticle. (*Bottom*) Metallic nanoparticle size distribution obtained by TEM image analysis (From reference [24])

over the sample. In fact, the alloys can crystallize in different phases (depending on the alloy composition), such as in ordered and substitutionally disordered form. Furthermore, it is difficult to obtain single phase nanoalloy crystals. So before EXAFS analysis, it is necessary to obtain a preliminary accurate morphological investigation and structural characterization.

Powder diffractometer is the instrument which performs powder diffraction measurements. Two measurement configurations in the diffractometers can be operated: in transmission (Debye-Scherrer configuration) and in reflection mode. The more common is the reflection one. It is based on filling the powder sample in a small container disk and its surface carefully leveled. The disk is putted on one diffractometer axis and tilted by an angle θ; in the meantime, a detector (scintillation counter) rotates around it on an arm at twice this angle. This is the Bragg-Brentano configuration. Theta-theta configuration represents another diffraction geometry consisting in a stationary position of the sample, while the X-ray tube and the detector are rotated around it. The angle formed between the tube and the detector is 2θ.

For example, in Fig. 4a, typical X-ray diffraction pattern is shown. The peaks represent the Bragg planes with Miller indexes (111) for the first peak, (200), (220), (311), and (222) of the Pt-Co nanomaterial. Peaks are smoother due to the nanosize of the sample. By identifying their position as a function of θ, it is possible to identify the crystalline structure and calculate the cell parameter of the sample.

XRD data analysis has been performed using the PEAKFIT and EDXRD programs that are part of the GNXAS package [9, 13, 28] for XAS/XRD analysis.

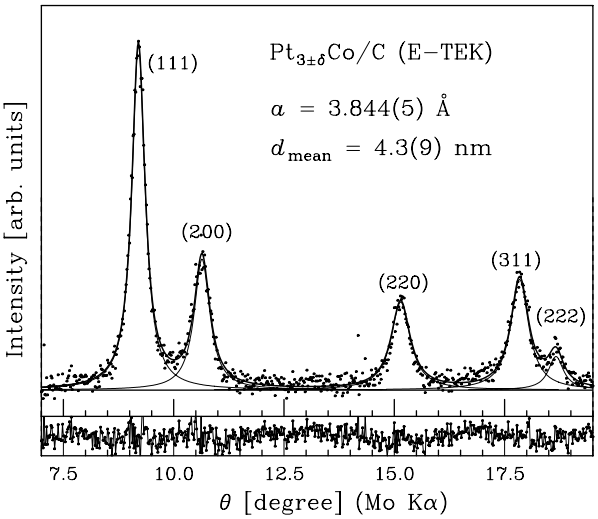

Fig. 4 X-ray diffraction pattern of platinum cobalt nanoparticle powder supported on Vulcan (E-TEK™). The calculated pattern was modeled using Voigt functions (*solid lines*), and experimental data (*points*) are compared. Residual diffraction pattern curve is shown below

Many factors determine the width B of a diffraction peak, including:

1. The presence of defects in the lattice
2. Instrumental factors
3. The crystallites size (peak width, Scherrer equation 13)
4. Strain differences in different grains

Pt-Co nanometric sample shows peaks' position characteristic of fcc structure nanoparticles. The crystalline phase is typical of a single phase because no additional peaks or shoulders are observed in the diffraction pattern.

From the cell parameter obtained can be evaluated also the Co atomic fraction, f_{Co}, by Vegard's law [29–31]:

$$f_{Co} = \frac{a - a_0}{a_s - a_0} f_s, \tag{19}$$

where a_o and a_s are the lattice parameters of pure Pt (0.3925 nm) and Pt-Co alloy (0.375 nm [32]), respectively. f_s is the reference Co alloy atomic fraction in Pt-Co ($f_s = 0.5$) [29, 33].

X-ray fluorescence spectroscopy is useful to know what chemical components that are present in a sample. The typical form of a fluorescence peak is sharp (shown in Fig. 5), and the spectral lines, shown in Fig. 5, are obtained by the wavelength-dispersive method (see Moseley's law).

Energy-dispersive analysis means that the fluorescent X-rays emitted are conducted from the material sample into a solid-state detector which yields a "continuous" distribution of pulses, whose voltages are proportional to the incoming photon energies. A multichannel analyzer (MCA) can process this signal producing a digital spectrum which can be converted to analytical data.

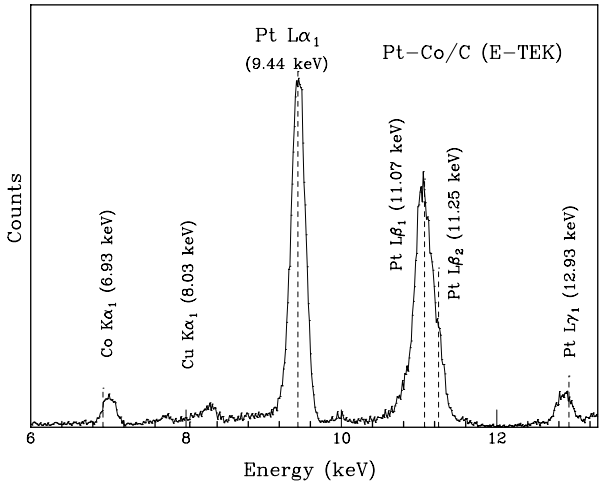

Fig. 5 Typical energy-dispersive XRF spectrum: spectra of Pt-Co powder (E-TEK™)

X-ray Absorption Measurements

XAS spectra could be acquired in two different modes: transmission and fluorescence modes. The X-ray absorption coefficient $\mu(E)$ of a material as a function of energy is measured by XAS. The sample is hit by X-rays. The incident and transmitted X-ray intensity is recorded when the incident X-ray energy is incremented. The transmitted number of X-ray photons through a sample (I_t) is equal to the number of X-ray photons irradiated on the sample (I_0) multiplied by a decreasing exponential depending on the atom type embedded in the sample structure, the absorption coefficient μ, and the thickness of the sample x: $I_t = I_0\, e^{-\mu x}$. The log ratio of the incident X-ray intensity to the transmitted X-ray intensity represents the absorption coefficient

$$\mu x = \log\left(I_0 / I_t\right) \tag{20}$$

In performing XAS, measurements in transmission mode are necessary to prepare pellets by slightly grinding sample hand mixing the powdered material with graphite in given proportions calculated with specific software (XASAM). Optimizing the absorption jump, the bulk absorption effects were minimized, improving the display of pre- and post-edge details. For example, the values obtained for a 30 % of Pt-Co and 70 % of Vulcan pellet with a diameter about 13 and 2 mm of thickness are shown in Table 2. Typical XAS signals obtained in transmission mode are shown in Fig. 6.

When the amount of the sample is very low, fluorescence XAS measurements are necessary, for example, during the in situ experiments, when the sample is not the pristine material as a powder but is an electrode.

Fluorescence mode means to measure fluorescence emitted by secondary electron falling to core level. In order to obtain reliable measurements in fluorescence mode, the amount of tested material in the sample has to be very low.

Table 2 XASAM program output: Information obtained for an optimal XAS jump, J is the jump obtained using the ρ(mg/cm^2) value in 30 % Pt-Co and 70 % of Vulcan (E-TEK) sample. The pellet has a surface area of approximately 1.32 cm^2. Multiplying the pellet area to ρ the result is the number of millgrams of the sample that have to be put in a mixture with high-purity graphite (Alfa Aesar)

Edge	E(eV)	$\sigma\left(\frac{\text{cm}^2}{\text{g}}\right)$ –	$\sigma\left(\frac{\text{cm}^2}{\text{g}}\right)$ +	J	$\rho\left(\frac{mg}{cm^2}\right)$	Opt. sam. size d(μm)
Pt L_1-edge	13,892	50.64	57.64	0.17	24.1	241.0
Pt L_2-edge	13,273	41.76	56.51	0.36	24.6	245.8
Pt L_3-edge	11,564	26.65	58.92	0.76	23.6	235.7
Co K-edge	7,709	67.25	77.41	0.18	17.9	179.4

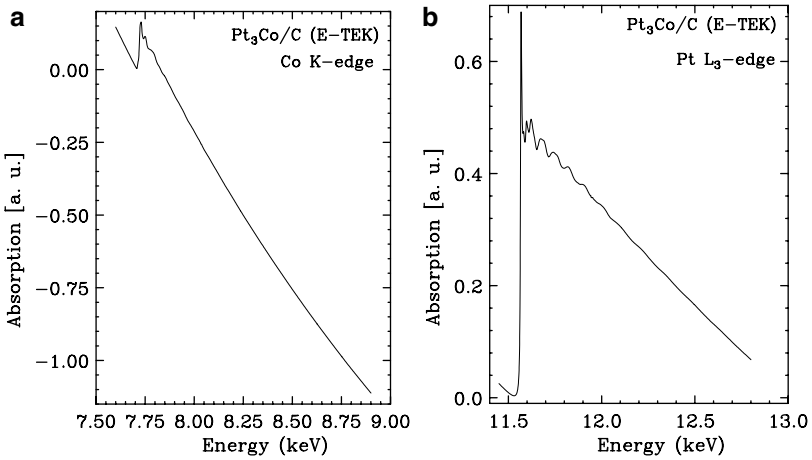

Fig. 6 30 % Pt-Co/C (E-TEK) X-ray absorption spectra measured at ELETTRA (Trieste); (**a**) Co K-edge, (**b**) Pt L_3-edge

In fact, the intensity measured by an X-ray fluorescence detector, $I_f(E)$, is related to the intensity of the incoming X-ray beam, $I_0(E)$, and the "X" atomic species absorption coefficient $\mu_X(E)$ is linear Refs. [34–36]:

$$I_f = \frac{I_0(E)(\Omega/4\pi)\varepsilon_X \mu_X(E)}{\mu_{tot}(E) + \mu_{tot}(E_f)\dfrac{\sin\phi}{\sin\theta}}\left[1 - e^{\left[-\frac{\mu_{tot}(E)}{\sin\phi} + \frac{\mu_{tot}(E_f)}{\sin\theta}\right]}\right] \tag{21}$$

where $\mu_{tot} = \mu_X + \mu_{oth}$ indicates the total linear absorption coefficient (μ_{oth} associated with other atoms within the sample), εX is the fluorescence produced by the photoabsorbing atom X, and $\Omega/4\pi$ is the solid angle with the detector (angles ϕ and θ are defined in Fig. 11b). In our experiments, μ_{tot} is associated with electrodes of very low catalyst loading. In this way, the transmission of the small thickness approximation can be applied to our case [1–3]. Within this limit, the exponential in Eq. 21 reduces to

$$\begin{aligned} 1 - \exp\left[\left(\frac{\mu_{tot}(E)}{\sin\phi} + \frac{\mu_{tot}(E-f)}{\sin\phi}\right)d\right] \\ \simeq \left(\frac{\mu_{tot}(E)}{\sin\phi} + \frac{\mu_{tot}(E-f)}{\sin\phi}\right)d \end{aligned} \tag{22}$$

Taking into account the approximation in Eq. 22 and the geometry used in this experiment $\left(\sin\phi = \sin\theta = \sqrt{2}/2\right)$, Eq. 21 becomes

$$I_f(E) = I_0(E)\frac{\Omega}{4\pi}\varepsilon_X \mu_X(E)\sqrt{2}d$$
$$\Rightarrow \mu_X(E) \propto \frac{I_f(E)}{I_0(E)} \tag{23}$$

The interpretation of the raw XAS data in relation with the catalytic layer is simplified by result in Eq. 23 without ulterior theoretical corrections. But, when there are high-absorbing catalyst supports and/or excessive catalyst loading, this approximation in Eq. 23 can fail. Working in fluorescence mode can be an advantage for the small thickness approximation; in fact, inhomogeneities of the sample do not severely affect the XAS measurements as in the transmission mode.

EXAFS Analysis and Effect of Chemical Disorder

This section presents an example of a detailed XAS structural investigation of nanocrystalline Pt-Co supported on Vulcan (E-TEK™, 30 % of metal and 70 % of an amorphous and porous phase of carbon called Vulcan), used as a catalyst material in fuel cell applications in order to show and explain the characterization method. Results obtained by TEM and XRD demonstrate that the Pt-Co/C sample can be treated as constituted by a homogeneous ensemble of $Pt_{3\pm\delta}Co$ fcc nanocrystalline particles with a mean diameter of ~5 nm. Moreover, the average local structure of Pt-Co/C can be assumed very similar to the bulk crystalline Pt_3Co (as for Pt nanoparticles [37]) confirmed by XAS, TEM, and XRD results.

The Pt_3Co alloy has an $L1_2$ structure (Cu_3Au-like) [32]. In this structure, Pt atoms are substituted by Co atoms at the corners of the crystal structure of the face-centered cubic (fcc). Using theoretical calculations of the X-ray absorption cross section with GNXAS method, the experimental EXAFS data have been analyzed [13, 28]. The theoretical XAS signal for various two-body and three-body configurations of a typical fcc $L1_2$ structure has been calculated, and the details are listed in [24].

In crystalline alloys of platinum cobalt chemical, disorder is present and the disorder degree depends on the thermal treatment and preparation procedures. A simple methodology to reproduce the effect of substitutional disorder was used to calculate the coordination numbers (CNs) and multiplicities of the multiple-scattering signals contributing to the EXAFS spectra.

Chemical disorder affects the CNs components (Pt-Co, Co-Pt, Co-Co and Pt-Pt first and farther neighbor). So with a simple computer simulation scheme, the multiplicities of the main local two-body and three-body fcc $L1_2$ configurations as a function of the degree of chemical disorder (see also Ref. [38]) have been calculated. This was obtained by introducing the occupation probabilities of the lattice sites. We have considered a $6\times6\times6$ supercell containing 216 fcc units (a=3.385 Å) for a total number of 864 atoms in order to minimize the effects of the finite size of our calculations.

By introducing a finite probability $0 \le p \le 1$ for the occupancy of selected lattice sites with Co atoms, substitutional disorder is simulated. In detail, p is taken as the probability that a Co atom occupies the site at the corner of the fcc cell ((0, 0, 0) position in each fcc unit, see Fig. 7a). While $(1-p)/3$ is the Co occupation probability

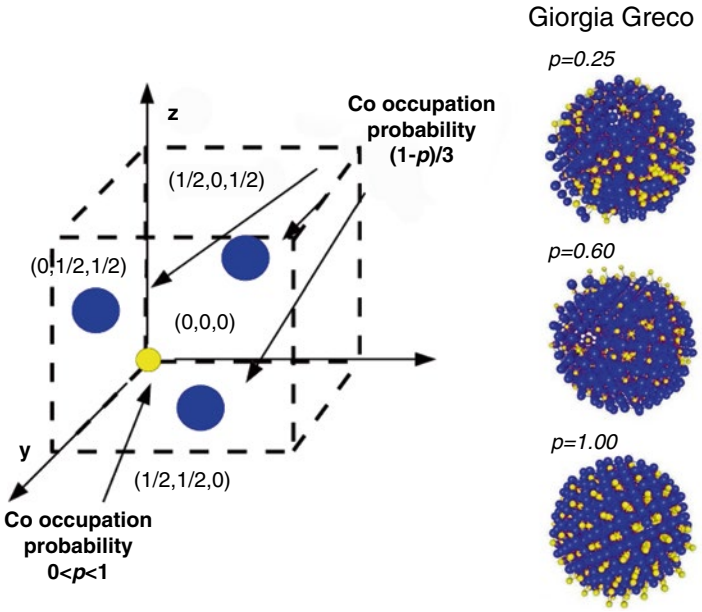

Fig. 7 (*Left side*) $L1_2$ primitive cell, the *arrows* indicate the Co occupation probability for every site. (*Right side*) Three different spherical nanocrystals with an fcc $L1_2$ structure and with a different degree of chemical disorder (From reference [24])

of any of the three other sites of the fcc unit ((1/2, 1/2, 0), (0, 1/2, 1/2), (1/2, 0, 1/2) positions). In this way for a great number of crystalline sites, the stoichiometry in the thermodynamic limit is preserved.

The range $0.25 < p < 1$ is considered in the calculation that includes from a completely ordered structure ($p = 1$) to a completely disordered one ($p = 0.25$, for which no preferential position can be defined for Co). Three examples of spherical clusters in Fig. 7b (obtained using selected cutoff radii for the supercells) and different chemical ordering p are shown. It has to be underlined that the model does not reproduce a real atomic structure and dynamics in nanocrystalline materials including grain boundaries.

We found that CNs and degeneracy associated with the amplitude of the MS XAS signals are deep influenced by the chemical disorder. In fact, some CNs drop to zero for the fully ordered structure, while most CNs and degeneracy are slowly varying for p lower than 0.4. An appropriate order parameter is defined as

$$s \frac{p - C_a}{1 - C_a}, \tag{24}$$

where p is the occupation probability defined above and C_a is the atomic concentration of the selected chemical species (1/4 for Pt_3Co). In this way, $s = 0$ indicates random occupancy ($p = 1/4$) and $s = 1$ perfect order.

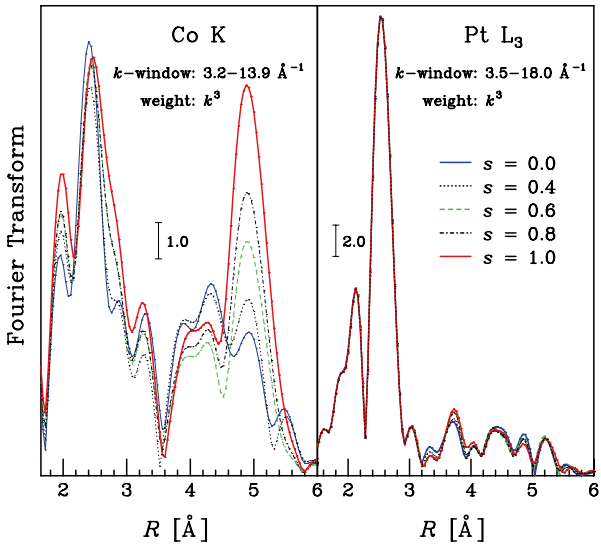

Fig. 8 (*Colors online*) Fourier transforms of the Pt L_3 and Co K theoretical XAS signals calculated for different values of the disorder parameter s (structural parameters optimized for the $Pt_{3\pm\delta}Co$ nanoalloy) (From reference [24])

The most evident changes are founded in the CNs/degeneracy of the fourth-shell atoms (180° configurations) that can be considered as flags for chemical ordering in these alloys (along with the presence of Co-Co first neighbors). Figure 8 shows the Fourier transforms (FTs) of the Pt L_3- and Co K-edge theoretical XAS signals calculated for different values of the disorder parameter s.

It has to be underlined that chemical disorder affects in particular the Co K-edge FT modifying the intensity of the FT peak around 5 Å that is associated with collinear configuration changes of a factor of 3 between the limiting cases $s=0$ and $s=1$. Moreover, nanoparticle size affects also the total CNs, so reduction (first neighbor CN is ~11 instead of 12 for particles with a mean size about 5 nm) due to the finite size effect is taken into account using other simulations performed for fcc nanoparticles [37]. All of these constraints guarantee a robust structural refinement for double-edge EXAFS data analysis of the nanocrystalline $Pt_{3\pm\delta}Co/C$ sample, using a total of 15 structural parameters over around 1000 experimental points and including all of the MS signals up to the fourth coordination shell [24].

Concluding and combining all results, the nanoparticle chemical disordering was found to be measurable with high accuracy. Moreover, compared to Pt, Co local structure is characterized by a higher level of structural disorder, verified also by the higher variances in interatomic distances.

This approach based on combining different state-of-the-art techniques allows us to conclude that it is robust and successful for nanomaterial characterization and is also appropriate for applications in structural refinements of any nanocrystalline active system. The mentioned above data analysis methodology is now applied for analyzing changes in local structure under in-operandi condition in a real fuel cell and during ageing process [39].

Conclusions

This chapter describes different characterization techniques such as TEM (transmission electron microscopy), XRD (X-ray diffraction), and in particular the site-selective XAS (X-ray absorption spectroscopy) that, when combined together in the correct way, represent a robust method for nanomaterial characterization. In this chapter, also a brief theoretical base of these techniques is presented. Particular evidence is given to XAS technique that permits not only a deep nanomaterial characterization (e.g., alloy chemical ordering identification) but also in situ characterization. An application of this method and this statement to Pt-Co nanomaterial used as catalyst in proton exchange membrane fuel cell is also presented.

Appendix

Design and Performances of the XAS PEM Fuel Cell

This section describes the experimental setup used to perform in cell measurements. For optimizing in situ XAS measurements on the catalyst during original electrochemical activity, a standard pemmican has been modified ad hoc [40]. In situ X-ray investigations of active materials first need to reduce the background absorption due to the various components of the cells. The thickness of the electrodes and membrane cell components has to be severely restricted if we would like to probe the valence and structure of metals participating in the catalytic process.

Due to this restriction, standard PEM fuel cells must be modified; the body of the cell was modified designing suitable windows for X-ray investigations. For obtaining XAS measurements in transmission mode with low noise, an EFC-05-02 (Electrochem) fuel cell was modified to achieve high transmission rates for photon energies in energy range about 515 keV, where the materials used as catalyst have most of the core levels.

The commercial fuel cell is made by two isotropic graphite separator plates, a 5 cm^2 active area (serpentine flow pattern) and two gold-plated current collectors. Eight screws keep together the plates of graphite; in this way, a high enough compression on the membrane electrode assembly (MEA) is induced providing a good electrical contact. In order to obtain maximum X-ray transmittance, two thin graphite windows (light and gas tight) are hollowed in the EFC-05-02 cells. The total graphite thickness obtained up to 0.25 mm, over a flat 1 mm × 7 mm area, providing a double window for XAS in transmission mode and possible X-ray fluorescence and X-ray diffraction measurements owing to the wide angular acceptance (~100° on the beam plane, ~5 % covered solid angle), as shown in Fig. 9. The X-ray window is positioned to be parallel (y) and in correspondence (z) with the serpentine channels (width 0.8 mm) in order to minimize absorption.

This modified cell allows standard condition XAS measurements at EXAFS beamlines with a typical beam size of ~ 0.4 mm × 5 mm. The cell position can be easily modified during the experiment in respect of beam, allowing the best geometry for the experimental technique in use. More details are listed in [40].

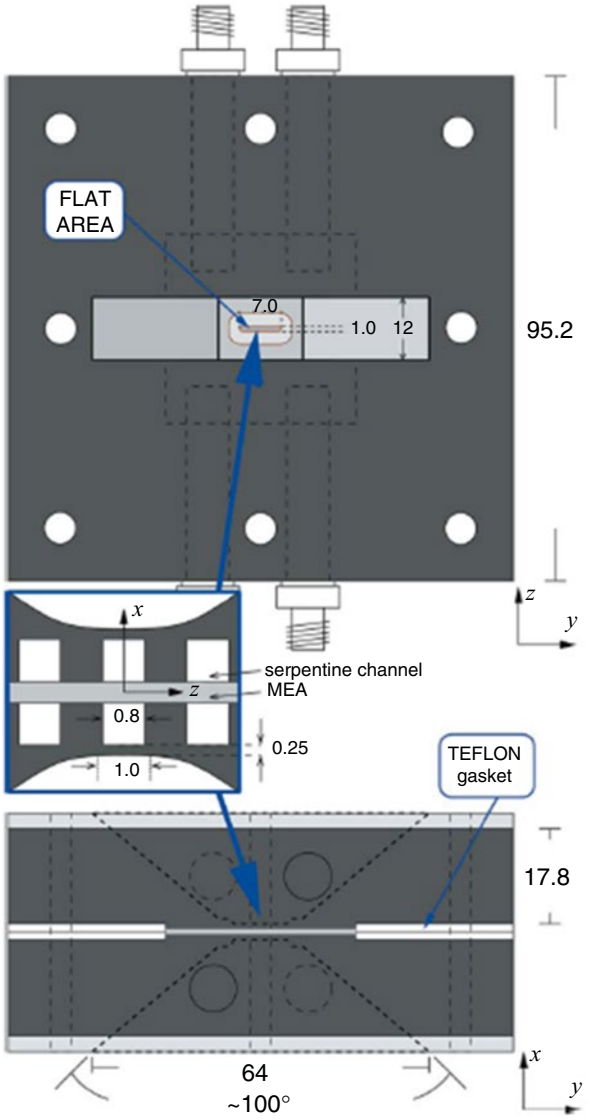

Fig. 9 Schematic view of the modified fuel cell optimized for in situ X-ray absorption measurements (front and side views, dimensions given in mm). The front view shows the drilling of the electrode of graphite in order to reduce the X-ray absorption saving space for the fuel channels (hydrogen and oxygen). Each graphite plate has a minimal thickness about 0.25 mm, thus minimizing the absorption along the X-ray path (x, see *inset*). The side view shows the wide angular aperture allowing for possible X-ray diffraction and X-ray fluorescence measurements; the cell MEA positioning is also shown (From reference [40])

Sample Preparation

Electrochemical and structural measurements were performed on electrodes. The catalytic layers were prepared using E-TEK 30 % Pt_3Co supported on Vulcan XC-72 powder (with total metal loading of about 1.0 mg/cm^2).

The metal loading was counted from the weight. Membrane electrode assemblies (MEAs) used to perform cathode catalyst degradation were composed of

Nafion® N-112R as a proton conductive membrane and Pd (30%Pd/Vulcan XC-72 powder, Pd loading 1.0 mg cm^{-2}) as an anode catalyst.

In the X-ray beam window region, a Pd counter electrode [41] was used in order to prevent perturbations of the electrical field on the catalyst under consideration [42, 43]. Before XAS measurements, each new MEA was subjected to conditioning process at a voltage of ~0.5 V for 15 min, and then Rapid Check cell performances by electrochemical cycles were done.

In Situ Experimental Setups

A typical setup for in situ XAS experiments in transmission mode at the BM29 (ESRF) or XAFS 11.1 (ELETTRA) beamlines is shown in Fig. 10. In those beamlines, the XAS fuel cell described before has been tested.

In a standard transmission configuration, the fuel cell has been positioned and aligned along the beam with motorized translation stages. The reference sample has been included for a more precise energy calibration. The cell channels for oxygen and hydrogen gas were connected to their lines working at 1.2 bar (the gas flow was set to ~100 ml min^{-1}). During XAS measurements, the voltage output was remotely controlled by a computer-driven potentiostat/galvanostat and continuously stored.

Figure 11 shows the setup, which allows measurements both in transmission and in fluorescence modes. Looking at Fig. 11, the fuel cell has been installed between the ionization chambers I_0 and I_1 at the X-ray spectrometer BM29 (ESRF) close to a 13-channel Ge X-ray detector (I_f). Figure 10 shows the setup schematic view, and it is possible to identify the fuel cell, the gas lines (humidified O_2 and H_2), the electrical connections necessary to operate the cell, and the X-ray fluorescence detector located on the left side. The pressure of the gases has been set to 1 atm; the gas flux

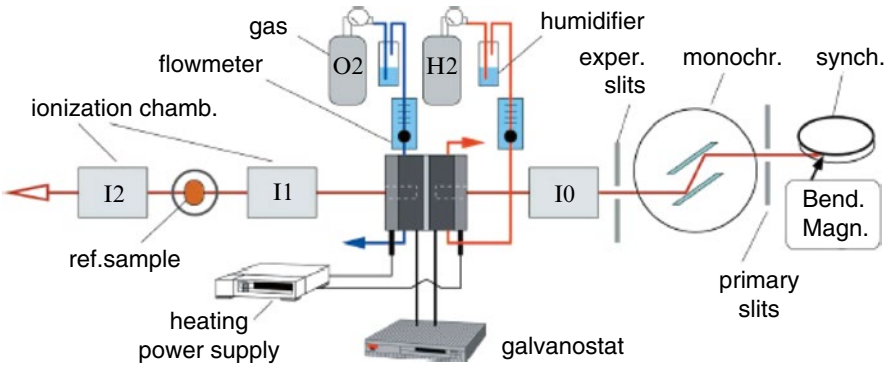

Fig. 10 Typical setup for XAS experiments on fuel cells under operating conditions (From reference [40])

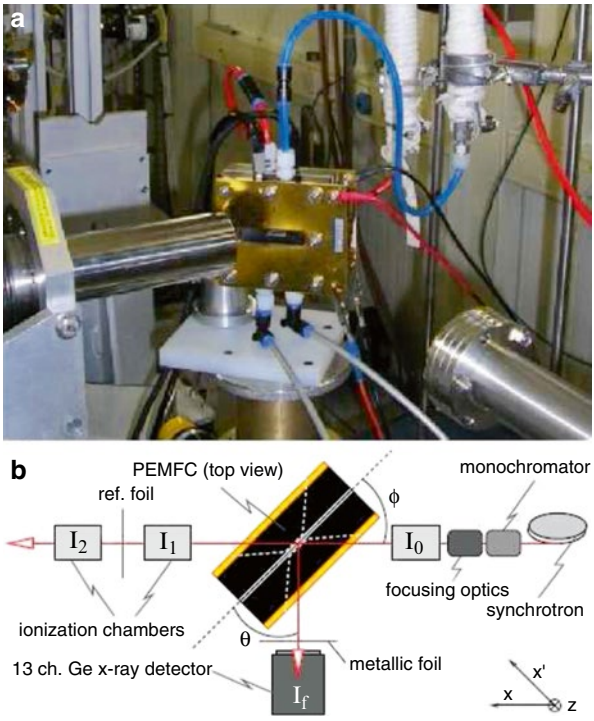

Fig. 11 (**a**) Picture taken at the BM29 beamline (ESRF) that shows the modified fuel cell positioned close to the 13-channel Ge X-ray detector (on the *left*) on the beam direction. (**b**) The schematic experimental setup top view $\theta = \phi = 45°$. The absorption coefficient $\mu(E)$ of selected atomic species embedded inside the electrode can be measured both in transmission mode ($\mu(E) = \ln(I_0/I_1)$) and in fluorescence mode ($\mu(E) \propto I_f/I_0$). The absorption coefficient of a reference sample is measured ($\mu(E) = \ln(I_1/I_2)$) at the same time

was about 100 ml min^{-1}. The fuel cell has been located with an angle of 45° with respect to the X-ray beam direction. In order to maximize the recovered solid angle, the multichannel detector has been positioned close to the cell at 90° to the incident beam in the synchrotron (horizontal) plane.

Taking advantage of this geometry and the twofold wide aperture machined on both sides of the cell, simultaneous XAS measurements in transmission and energy-dispersive fluorescence (EDXRF) mode can be carried out (see Fig. 11) without further alignment.

So make the most of this geometry simultaneous XAS measurements in transmission and energy-dispersive fluorescence (EDXRF) mode can be carried out (see Fig. 11) without further alignment. The quality of the carried-out signals is really good as shown in Fig. 12 where extracted EXAFS signals of Pt-Co nanocatalyst at different potentials are presented for both ages. It has also to be underlined that the Co quantity in the electrode is very few (0.1 mg/cm^2) in spite of the quality of the signal being more than satisfactory

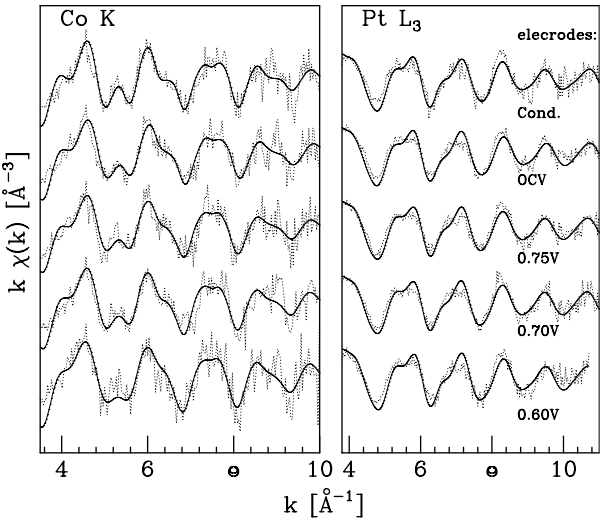

Fig. 12 30 % Pt-Co/C electrode in situ EXAFS signals at different potentials. Starting from the *top* of the figures: electrode conditioned, at OCV, 0.75, 0.70, and 0.60 V. *Dotted lines* represent the experimental signals and the *solid lines* the theoretical ones

References

1. Lee PA, Citrin P, Eisenberger P, Kincaid B (1981) Extended x-ray absorption fine structure–its strengths and limitations as a structural tool. Rev Mod Phys 53:769
2. Teo BK, Joy DC (1981) EXAFS spectroscopy, techniques and applications. Plenum, New York
3. Hayes TM, Boyce JB (1982) EXAFS spectroscopy. In: Eherenreich H, Seitz F, Turnbull D (eds) Solid state physics advances in research and applications, vol 37. Academic, New York, p 173
4. Koningsberger DC, Prins R (eds) (1988) X-ray absorption: principles, applications, techniques of EXAFS, SEXAFS, and XANES. Wiley, New York
5. Sayers DE, Stern EA, Lytle FW (1971) New technique for investigating noncrystalline structure: fourier analysis of the EXAFS. Phys Rev Lett 27:1204
6. Stern EA, Sayers DE, Dash JG, Shechter H, Bunker B (1977) Adsorbate and substrate characterization using extended X-ray absorption fine structure. Phys Rev Lett 38:767
7. Stern EA, Heald SM, Bunker B (1979) Amplitude of the extended-X-ray-absorption fine structure in bromine molecules. Phys Rev Lett 42:1372
8. Citrin H, Eisenberger P, Kincaid BM (1976) Transferability of phase shifts in EXAFS. Phys Rev Lett 36:1346
9. GNXAS (2009) In: Di Cicco A (ed) Extended suite of programs for advanced X-ray absorption data-analysis: methodology and practice. TASK Publishing, Scientific Bulletin of Academic Computer Center in Gdansk, Poland. ISBN 978-83-908112-8-4
10. Benfatto M, Natoli CR, Bianconi A, Garcia J, Marcelli A, Fanfoni M, Davoli I (1986) Multiple-scattering regime and higher-order correlations in x-ray-absorption spectra of liquid solutions. Phys Rev B 34:5774
11. Natoli R, Benfatto M (1986) A unifying scheme of interpretation of X-ray absorption spectra based on the multiple scattering theory. J Phys (Paris) Colloq 47:C8–C11

12. Tyson TA, Hodgson KO, Natoli CR, Benfatto M (1992) General multiple-scattering scheme for the computation and interpretation of x-ray absorption fine structure in atomic clusters with applications to SF_6, $GeCl_4$, and Br_2 molecules. Phys Rev B 46:5997
13. Filipponi A, Di Cicco A (1995) X-ray absorption spectroscopy and n-body distribution functions in condensed matter ({I}): theory. Phys Rev B 52:15122
14. Filipponi A, Di Cicco A, Natoli CR (1995) Multiple-scattering analysis of the X-ray absorption spectrum of Os 3 (CO) 12 carbonyl cluster. Phys Rev B 52:15135
15. Azroff LV, Kaplow R, Kato N, Weiss RJ, Wilson AJC, Young RA (1974) X-ray diffraction. McGraw-Hill, New York, US
16. Langford J, Wilson A (1978) Scherrer after sixty years: a survey and some new results in the determination of crystallite size. J Appl Cryst 11:102–113
17. Cowley JM (1995) Diffraction physics. Elsevier Science BV, Amsterdam, The Netherlands
18. Fultz B, Hove J (2007) Transmission electron microscopy and diffractometry of materials. Springer, Berlin, Germany
19. Kirkland E (1998) Advanced computing in electron microscopy. Springer, New York, US
20. Neumann W, Hillebrand R, Werner P (1897) Electron microscopy in solid state physics. Elsevier, Amsterdam
21. Zou XD (1995) Electron crystallography of inorganic structures. Theory and practice. PhD thesis, Stockholm University
22. Cowely JM (1993) Electron diffraction technique, high resolution imaging. International Union Crystallography. Oxford University Press, Oxford, pp 131–169
23. Kilhborg L (1995) Phase contrast and high resolution electron microscopy. Department of Inorganic Chemistry, Stockholm University, Sweden
24. Greco G, Witkowska A, Principi E, Minicucci M, Di Cicco A (2011) Local ordering of nanostructured Pt-Co probed by multiple-scattering XAFS. Phys Rev B 83(13):134103
25. Gontard LC, Chang LY, Hetherington CJD, Kirkland AI, Ozkaya D, Dunin-Borkowski RE (2007) Aberration-corrected imaging of active sites on industrial catalyst nanoparticles. Angew Chem 46:3683
26. Chen S, Sheng W, Yabuuchi N, Ferreira PJ, Allard LF, Shao-Horn Y (2009) Enhanced activity for oxygen reduction reaction on "Pt_3Co" nanoparticles: direct evidence of percolated and sandwich-segregation structures. J Phys Chem C 113(3):1109–1125
27. Menguy N (2007) Microscopes electroniques. Online transparencies http://www.impmc.jussieu.fr/menguy/Cours.html
28. Filipponi A, Di Cicco A, Zanoni R, Bellatreccia M, Sessa V, Dossi C, Psaro R (1991) X-ray absorption spectroscopy and n-body distribution functions in condensed matter ({II}): data-analysis and applications. Chem Phys Lett 184:485
29. Vegard L (1921) Die konstitution der mischkristalle und die raumfüllung der atome. Z Phys 5(1):17
30. Denton AR, Ashcroft NW (1991) Vegard's law. Phys Rev A 43(6):3161
31. Urusov VS (1992) A geometric model of deviations from Vegard's rule. J Struct Chem 33:68–79
32. Hansen M (1958) Constitution of binary alloys. McGraw-Hill, New York
33. Zignani SC, Antolini E, Gonzalez ER (2008) Evaluation of the stability and durability of Pt and Pt–Co/C catalysts for polymer electrolyte membrane fuel cells. J Power Sources 182:83
34. Pfalzer P, Urbach J-P, Klemm M, Horn S, DenBoer ML, Frenkel AI, Kirkland JP (1999) Elimination of self-absorption in fluorescence hard-x-ray absorption spectra. Phys Rev B 60:9335
35. Tröger L, Arvanitis D, Baberschke K, Michaelis H, Grimm U, Zschech E (1992) Full correction of the self-absorption in soft-fluorescence extended x-ray-absorption fine structure. Phys Rev B 46:3283
36. Eisebitt S, Boske T, Rubensson J-E, Eberhardt W (1993) Determination of absorption coefficients for concentrated samples by fluorescence detection. Phys Rev B 47:14103
37. Witkowska A, Di Cicco A, Principi E (2007) Local ordering of nanostructured Pt probed by multiple-scattering XAFS. Phys Rev B 76:104–110

38. Lu ZW, Wei S-H, Zunger A (1992) Electronic structure of ordered and disordered Cu_3Au and Cu_3Pd. Phys Rev B 45:10314
39. Greco G, Witkowska A, Minicucci M, Olivi L, Principi E, Dsoke S, Moretti A, Marassi R, Di Cicco A (2012) Local ordering changes in Pt–Co nanocatalyst induced by fuel cell working conditions. J Phys Chem C 116(23):12791–12802
40. Principi E, Di Cicco A, Witkowska A, Marassi R (2007) Performance of a fuel cell optimized for in situ X-ray absorption experiments. J Synch Rad 14:276–281
41. Viswanathan R, Hou G, Liu R, Bare S, Modica F, Mickelson G, Segre C, Leyarovska N, Smotkin E (2002) In-situ XANES of carbon-supported Pt-Ru anode electrocatalyst for reformate-air polymer electrolyte fuel cells. J Phys Chem B 106:3458–3465
42. Roth C, Martz N, Buhrmester T, Scherer J, Fuess H (2002) In-situ XAFS fuel cell measurements of a carbon-supported Pt–Ru anode electrocatalyst in hydrogen and direct methanol operation. Phys Chem Chem Phys 4:3555–3557
43. Roth C, Benker N, Buhrmester T, Mazurek M, Loster M, Fuess H, Koningsberger D, Ramaker D (2005) Determination of O[H] and CO coverage and adsorption sites on PtRu electrodes in an operating PEM fuel cell. J Am Chem Soc 127:14607–14615
44. Durham J, Pendry JB, Hodges CH (1981) XANES: Determination of bond angles and multi-atom correlations in order and disordered systems. Solid State Commun 38:159
45. Durham J (1988) X-ray absorption: principles, applications, techniques of EXAFS, SEXAFS, and XANES (Ref. 2), p 53
46. Kizler P (1991) Three-body correlations in the metallic glass $Ni_{81}B_{19}$ probed by x-ray-absorption near-edge-structure spectroscopy. Phys Rev Lett 67:3555